nature nanotechnology

SUPPLEMENTARY INFORMATION

https://doi.org/10.1038/s41565-018-0252-6

In the format provided by the authors and unedited.

Electrical tuning of elastic wave propagation in nanomechanical lattices at MHz frequencies

Jinwoong Cha[1,2] **and Chiara Daraio**[2*]

[1]Department of Mechanical and Process Engineering, ETH Zurich, Zurich, Switzerland. [2]Engineering and Applied Science, California Institute of Technology, Pasadena, CA, USA. *e-mail: daraio@caltech.edu

Supplementary Information for
Electrical tuning of elastic wave propagation in nanomechanical lattices at MHz frequencies

Authors: Jinwoong Cha[1,2], Chiara Daraio[2*]

Affiliations:

[1]Department of Mechanical and Process Engineering, ETH Zurich, Switzerland
[2]Engineering and Applied Science, California Institute of Technology, Pasadena, CA, USA
*Correspondence to: Prof. Chiara Daraio (daraio@caltech.edu)

1. Tuning mechanisms

Here, we qualitatively discuss the frequency tuning mechanism of a single resonator. We assume the dynamics of a thin circular plate resonator can be described by the Von-Karman plate theory [S1], relevant for thin plates. The equation of motion for a single resonator, can be then written as:

$$\rho h \frac{\partial^2 W}{\partial t^2} + D\nabla^4 W - h\nabla\bullet(\underline{\boldsymbol{\sigma}}\nabla W) = F_e \ , \tag{S1}$$

where ρ, h, W, and D are the density, the plate thickness, the displacement field, and bending rigidity, $D=Eh^3/12(1-\nu^2)$, respectively. $\underline{\boldsymbol{\sigma}}$ is an in-plane stress tensor, which contains the contributions from the intrinsic residual stress, $\boldsymbol{\sigma}_0$, and the stress induced by the plate's deformation, $\boldsymbol{\sigma}_{induced}$. $F_e=\varepsilon_0 V^2/2(d-W)^2$ is the electrostatic force per unit area applied to the plate, where V is the applied voltage and d is the vacuum gap. Considering an axisymmetric deformation, the equation of motion can be reduced to:

$$\rho h \frac{\partial^2 W}{\partial t^2} + D\frac{\partial^4 W}{\partial r^4} - \left[\frac{\partial^2 W}{\partial r^2}\left(\frac{\partial F}{r\partial r}\right) + \frac{\partial W}{r\partial r}\left(\frac{\partial^2 F}{\partial r^2}\right)\right] = F_e \ . \tag{S2}$$

Here, F is an in-plane stress function that satisfies the following compatibility equation:

$$\frac{1}{Eh}\frac{\partial^4 F}{\partial r^4} = -\frac{\partial^2 W}{\partial r^2}\left(\frac{\partial W}{r\partial r}\right). \tag{S3}$$

We can express the displacement $W(\boldsymbol{r},t)$ as the summation of a dynamic displacement $W_D(\boldsymbol{r},t)$ and a static displacement $W_0(\boldsymbol{r})$. Provided that the dynamic displacement is much smaller than the static displacement when subject to an applied DC voltage, the electrostatic force can be approximated as:

$$F_e \approx \frac{\varepsilon_0 V^2}{2(d-W_0)^2}\left(1+\frac{2W_D}{d-W_0}\right). \tag{S4}$$

Therefore, the governing equation can be decomposed into a static part and a dynamic part.

$$\begin{gathered} D\frac{\partial^4 W_0}{\partial r^4} - \left[\frac{\partial^2 W_0}{\partial r^2}\left(\frac{\partial F}{r\partial r}\right) + \frac{\partial W_0}{r\partial r}\left(\frac{\partial^2 F}{\partial r^2}\right)\right] = \frac{\varepsilon_0 V^2}{2(d-W_0)^2} \\ \text{with} \quad \frac{1}{Eh}\frac{\partial^4 F}{\partial r^4} = -\frac{\partial^2 W_0}{\partial r^2}\left(\frac{\partial W_0}{r\partial r}\right) \end{gathered} \tag{S5}$$

$$\rho h\frac{\partial^2 W_D}{\partial t^2} + D\frac{\partial^4 W_D}{\partial r^4} - \left[\frac{\partial^2 W_D}{\partial r^2}\left(\frac{\partial F}{r\partial r}\right) + \frac{\partial W_D}{r\partial r}\left(\frac{\partial^2 F}{\partial r^2}\right)\right] - \frac{\varepsilon_0 V^2}{(d-W_0)^3}W_D = 0 \tag{S6}$$

If we assume that the dynamic displacement is too small to induce an in-plane stress, the in-plane stress function F can be assumed to be just a function of the static displacement field $W_0(\boldsymbol{r})$. Consequently, the static and the dynamic parts can be decoupled as in Equations S5 and S6. First, we can calculate the static deflection, $W_0(\boldsymbol{r})$, and the in-plane stress function, F, under any applied DC voltages. Then, the corresponding eigenfrequency can be found from the dynamic part applying appropriate boundary conditions. The third and fourth terms in Eq. S6 denote the tension induced stiffening, while the fifth term in Eq. S6 denotes the electrostatic softening.

Each eigenfrequency of the plate changes as a DC voltage is applied. The application of the voltage deflects the plate, changing its equilibrium configuration by inducing a radial tension inside the plate. This tension introduces a softening potential term $-\varepsilon_0 V^2/(d - W_0)^3$ in the dynamic representation of the system.

Solving analytically Eqs. S5 and S6 is difficult. Thus, we numerically solve the problem using COMSOL multi-physics. Instead of solving the Von-Karmann equations, COMSOL allows us to solve more general plate equations obtained from the Mindlin-plate theory [S1]. The Mindlin-plate theory converges to the Von-Karmann theory when the thickness of a plate becomes much smaller than the radius of the plate. Thus, the in-plane inertia of the plate (or displacement) can be neglected. We perform pre-stress eigen-frequency analyses for a circular plate with clamped boundary conditions by considering geometric nonlinearity. The radius of the plate is fixed to 5 μm for all performed simulations and we vary the thickness, t , and the vacuum gap distance, d , at different applied gate voltages.

As shown in Figure S1, thin plates with 5 nm and 10 nm thickness suspended with 600 nm vacuum gap present hardening behaviors, increasing the resonance frequency with the applied gate voltage. In this case, the contribution of the induced tension overcomes the electrostatic softening potential. The contribution from the induced tension decreases when the thickness increases, because the increased bending stiffness reduces the induced deformations. In contrast, thicker plates with 60 nm and 100 nm thickness suspended over a 200 nm vacuum gap present the decrease of the resonance frequency due to softening effects.

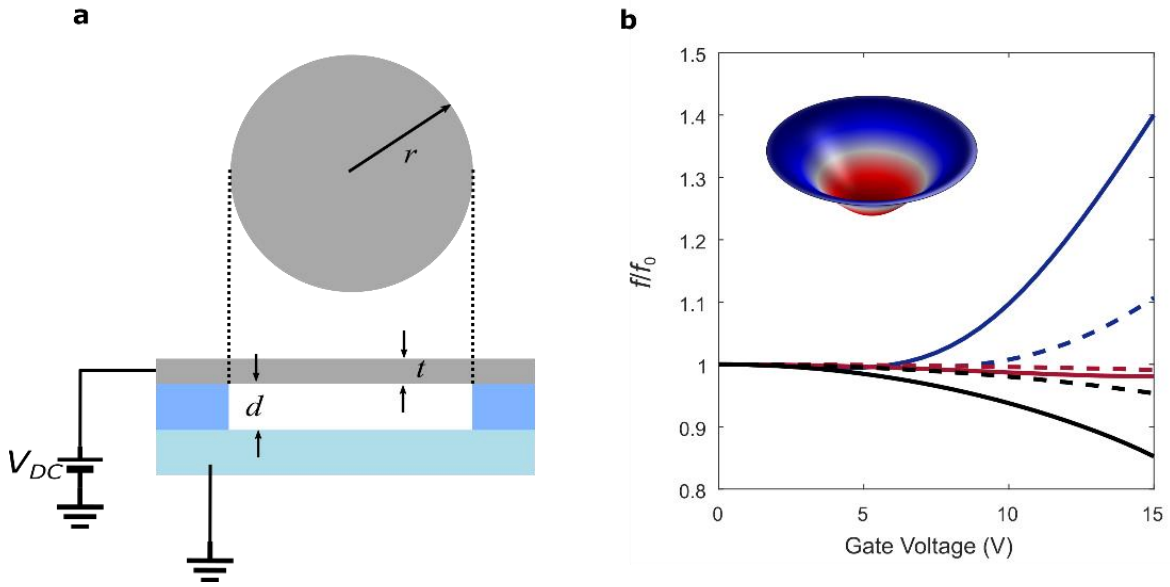

Supplementary Figure 1. Thickness and vacuum gap dependence of the eigenfrequency of the first normal mode in a suspended, circular plate. (**a**) Schematic of a voltage-gated circular plate with radius *r*, thickness *t*, and vacuum gap *d*. (**b**) The resonance frequency of the fundamental plate mode as a function of the applied DC gate voltage. The radius *r* is fixed to 5 μm. Blue solid (dashed) line: t = 5nm, d = 600nm (t = 10nm, d = 600nm). Red solid (dashed) line: t = 40nm, d = 400nm (t = 80nm, d = 400nm). Black solid (dashed) line: t = 60nm, d = 200nm (t = 100nm, d = 200nm).

2. Dependence of the dynamic response on the lattice spacing

To study the effects of different lattice periodicities on the dynamic response of the system, we experimentally measure the frequency responses of lattices without electrodes (Fig. S2). The frequency response for a one-dimensional lattice with lattice spacing a = 7 μm presents a clear band gap that separates acoustic and optical branches. Due to the clamping boundaries, which act as a grounding potential, the acoustic branch starts at 12 MHz. A decrease of lattice periodicity leads to a reduction in the size of the band gap, broadening acoustic and optical branches, as seen for a = 6 μm and 5 μm. The starting frequencies of the acoustic branch are 11 MHz for a = 6 μm and 10 MHz for a = 5 μm. The band gap between the acoustic and optical branches up-shifts with decreasing lattice spacing and the band gap size decreases. This decrease of the band gap size originates from the decrease of mass, an increase of bending stiffness and a decrease of the contrast of the equivalent rotational couplings G and H (see supplementary section 7). Further decrease of the periodicity leads to the vanishing of the band gap in the measurement range. In addition, below a 4 μm spacing, the lower acoustic band edge maintains a constant frequency, around 9.8 MHz. The increase of the distances between resonance peaks in Fig. S2a (for a=2 μm) is the clear evidence of the broadening of the acoustic branch, meaning that the strip width becomes uniform.

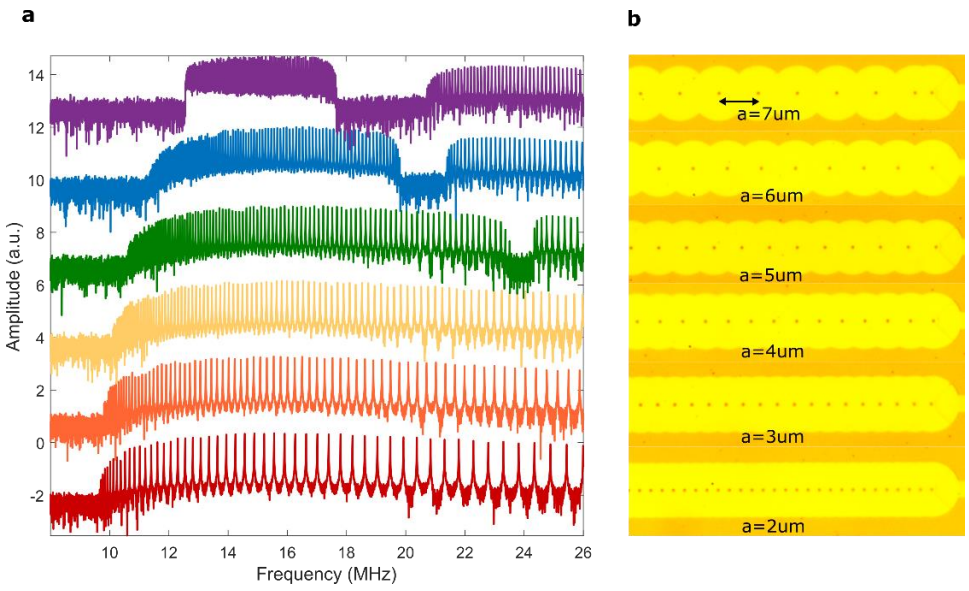

Supplementary Figure 2. Dependence of the phononic dispersion on periodicity. (**a**) Frequency responses of lattices with different periodicity ranging from a = 2 μm to 7 μm, measured at the end unit of each lattice. Here no tuning electrode is deposited. (**b**) Corresponding optical microscope pictures to the frequency spectrums in (**a**).

3. Effective gap distance for electrostatic force model

Due to the presence of a SiN_x layer under the tuning electrodes, we should consider the capacitive effect of the SiN_x layer in addition to the vacuum gap, *d*. We account for both electrostatic contributions by defining an effective gap distance d_{eff}, to model a negative elastic foundation in a finite element model. The electrostatic force per unit area is given by

$$F_e = -\frac{\partial E_{static}}{\partial d} = -\frac{V^2}{2}\frac{\partial C}{\partial d} \text{ with } C = \left(\frac{1}{C_{SiN_x}} + \frac{1}{C_{vac}}\right)^{-1} = \frac{\varepsilon\varepsilon_0}{t+\varepsilon d}\ , \tag{S7}$$

where $E_{static,}$ is the total electrostatic energy stored in the vacuum gap and the SiN_x layer, *V is* the applied gate voltage, *C* the total capacitance, *d* the vacuum gap distance, C_{SiNx} the capacitance of the SiN_x layer, C_{vac} the capacitance of the vacuum gap, ε_0 the vacuum permittivity, ε the dielectric constant of the SiN_x layer, and, *t*, the thickness of the SiN_x layer. The electrostatic force applied to the electrode on the SiN_x layer is then given by

$$F_e = -\frac{V^2}{2}\frac{\partial C}{\partial d} = \frac{\varepsilon^2\varepsilon_0 V^2}{2(t+\varepsilon d)^2} = \frac{\varepsilon_0 V^2}{2(d_0 + \frac{t}{\varepsilon} - W)^2} = \frac{\varepsilon_0 V^2}{2(d_{eff} - W)^2}\ , \tag{S8}$$

$$\text{with}\frac{\partial C}{\partial d} = -\frac{\varepsilon^2\varepsilon_0}{(t+\varepsilon d)^2}\ .$$

Equation S8 shows that the effective gap distance is defined as $d_{eff} = d_0 + t/\varepsilon$, where d_0 is the initial vacuum gap distance. To calculate the effective gap distance, d_{eff}, we consider the following example. When SiN_x with thickness t = 100 nm and dielectric constant ε = 7 is suspended with vacuum gap d_0 = 150 nm, over the grounded Si substrate, the total distance from the substrate to the tuning electrode is 250 nm. The effective gap distance is then calculated as d_{eff} =164 nm, which is 14 nm thicker than the vacuum gap distance, d_0. We can express the total displacement *W* as the sum of the static W_S and the dynamic W_D displacements. The electrostatic force with the effective gap distance is given by

$$F_e = \frac{\varepsilon_0 V^2}{2(d_{eff} - W)^2} = \frac{\varepsilon_0 V^2}{2(d_{eff} - W_s)^2}\left(1 - \frac{W_D}{d_{eff} - W_s}\right)^{-2}\ . \tag{S9}$$

Assuming that the dynamic displacement is much smaller than $d_{eff} - W_S$, the force can be approximated as

$$F_e = \frac{\varepsilon_0 V^2}{2(d_{eff} - W_s)^2} \sum_{n=1}^{\infty} n \left(\frac{W_D}{d_{eff} - W_s} \right)^{n-1} \approx \frac{\varepsilon_0 V^2}{2(d_{eff} - W_s)^2} \left(1 + \frac{2W_D}{d_{eff} - W_s} \right). \quad \text{(S10)}$$

4. Effects of the number of unit cells

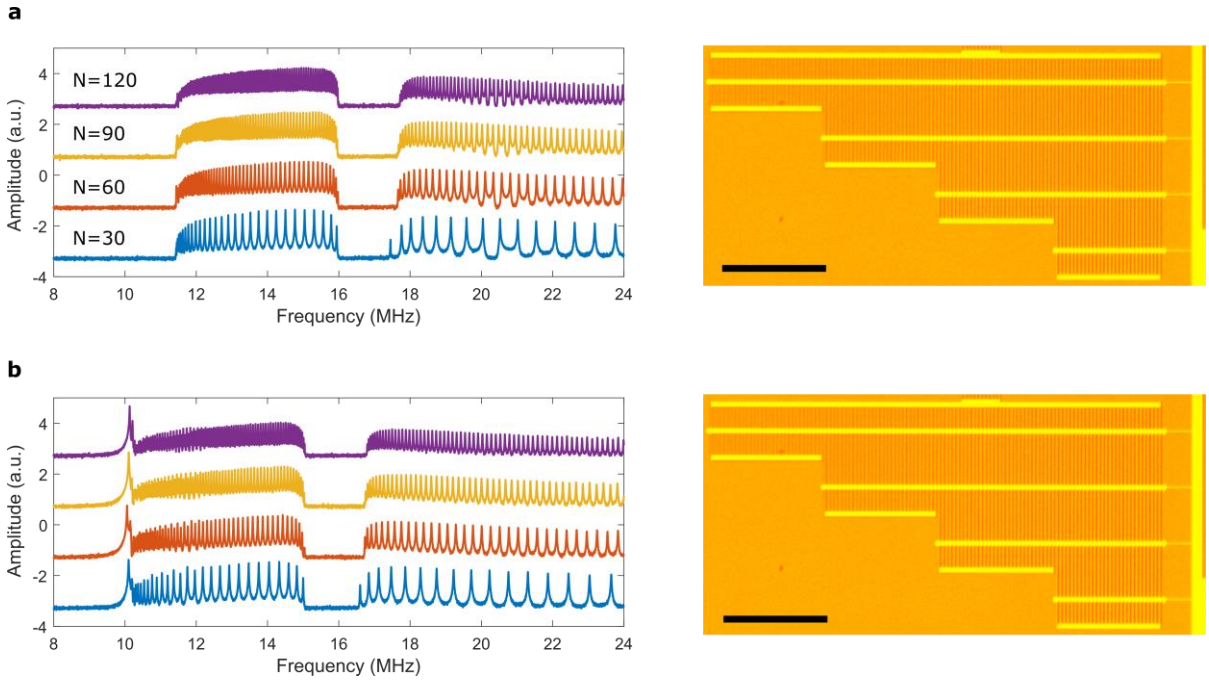

Supplementary Figure 3. Effects of the number of unit cells on the frequency response. (**a**), (**b**) Frequency responses of lattices with different number of unit cells N = 30, 60, 90, and 120 and the corresponding samples under an optical microscope. Scale bars, 200 μm. The applied gate voltages are 0 V for (**a**), and 20 V for (**b**).

Figure S3 shows the frequency responses of lattices with different numbers of unit cells N = 30, 60, 90, and 120, for gate voltages V_T = 0 V and 20 V. The lattice with N = 30 already shows a clear band gap ranging from 16 MHz to 17.8 MHz at V_T = 0 V, from 15 MHz to 16.8 MHz at V_T = 20 V. For the lattice with N = 30, we are able to detect the defect mode from the excitation unit around 17.6 MHz at V_T = 0 V (and at 16.4 MHz at V_T = 20 V), which appears near the band edge of the optical branch. However, this defect mode disappears in the lattice with N = 60. The spectrum

becomes more compact with an increased number of resonance peaks, as we increase the number of unit cells. The frequency ranges of the all the spectra measured are almost identical, regardless of the position on the lattice on the substrate, suggesting extremely uniform film properties and HF etching.

5. Experimental frequency dispersions

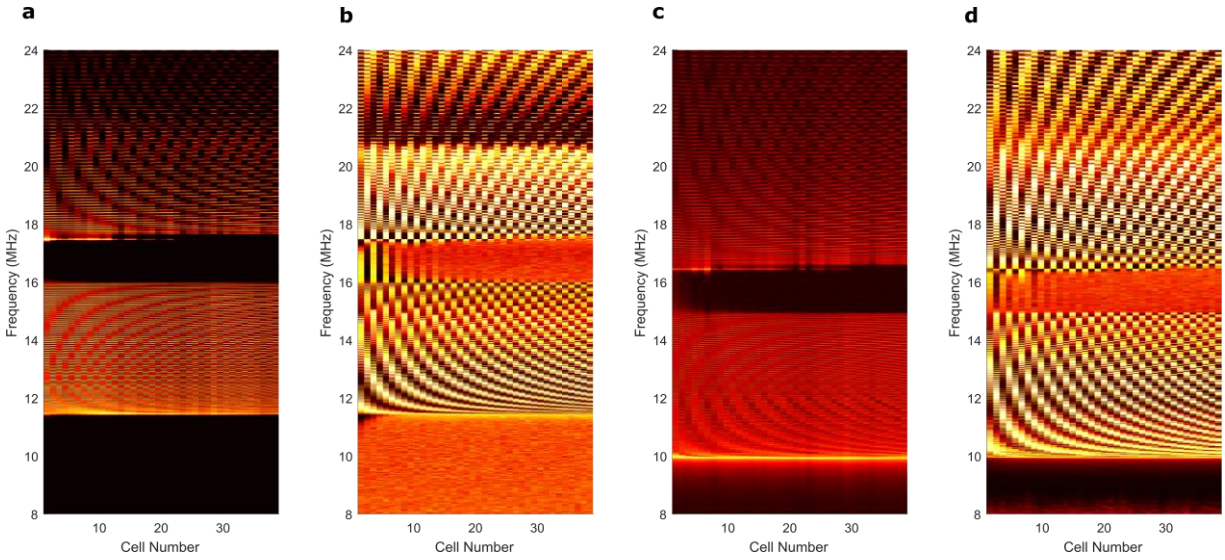

Supplementary Figure 4. Spatial scanning data. The frequency response of 40 unit cells at (**a**) V_T= 0 V and (**c**) V_T= 20 V. Log_{10}(amplitude) × sin(phase) frequency spectrums at (**b**) V_T= 0 V and (**d**) V_T= 20 V.

In our experiments, the dispersion curves are obtained from the frequency response of the lattice, measured by scanning a laser interferometer along the lattice. The scanning step is the same as the periodicity of the lattice, a = 7 μm. The number of scanned unit cells is 40. The lock-in amplifier enables the measurements of both the amplitude and the phase, with respect to the phase of the excitation source. To obtain the dispersion curves, we multiply sin(phase) or cos(phase) to the amplitude data (Fig. S4a for V_T = 0 V and S4c V_T = 20 V) in the frequency domain and perform a fast-Fourier transformation of the spatially scanned data.

Figure S4 shows a clear difference between the amplitude only data and the amplitude/phase data. We can observe the different spatial oscillation periods at different frequencies. For the acoustic branch, the lower frequency has the longer spatial period. The spatial period becomes shorter as the frequency approaches the band edge (~16 MHz in Fig. S4b and ~15 MHz in Fig. S4b) of the acoustic branch. In Figure S4b and S4d, we also observe the evanescent

behavior in the band gap region, meaning that some energy still propagates into several unit cells of the lattice. The lowest frequency of the optical branches exhibits the shortest spatial period. This means that the frequency is located at the zone boundary ($q = \pi/a$) of the Brillouin zone. Such information cannot be obtained from the amplitude response.

6. Measurement of the group velocity

To measure the group velocity in the lattice, we use an oscilloscope (Tektronix, DPO3034) instead of the lock-in amplifier. The oscilloscope allows us to directly measure waves in the time-domain. However, the noise floor of the photodetector makes the wave signals invisible if the amplitude is very low. Thus, we pre-filter the RF-output signals from the detector using a passive band-pass filter with 6 MHz – 22 MHz bandwidth. We then average 512 data in the time-domain. To excite the system, we send a chirped signal with a frequency spectrum ranging from 8 MHz to 22 MHz, using an arbitrary wave generator implemented in the lock-in amplifier. The frequency range of the chirped signal is enough to cover the broad frequency ranges that include the acoustic branches and the optical branches of our NEML. We apply V_{DC} = 20 V, and $V_{chirp,\,peak}$ = 375 mV to the excitation electrode. We measure the transient motion of the end unit of the lattice. The transient responses contain broad-band signals covering all the phononic modes within the frequency spectrum. To examine the group velocities at single frequencies, we apply a Burtterworth filter with 200 kHz bandwidth to the frequency responses.

7. Analytical model for frequency dispersion

We model our nanoelectromechanical lattice using a discrete element model consisting of two identical rigid plates in a unit cell (Fig. S5). Although a number of membrane modes lead to many frequency bands as a result, this diatomic picture can be justified since we measure the responses from two frequency branches in the experiments.

We assume that the plate elements are mounted on uniformly distributed nonlinear elastic foundations. The transverse nodal displacement of i^{th} node of n^{th} unit cell and the beam rotation with respect to i^{th} node of n^{th} unit cell are denoted by $u_{n,i}$ and $\theta_{n,i}$. To calculate the frequency dispersion, we consider a linearized parameter, $k_{nl,}$ of the nonlinear elastic foundations. This term includes the contributions from the clamped boundaries and the tunable electrostatic on-site potentials. We also consider an on-site rotational potential, J. We also consider the tension T in the model, to investigate the effects of intrinsic stress along the lattice. The wide and narrow regions of a unit cell of a real sample are modelled with two rotational springs with coupling strengths G

and *H* (Fig. S5). The presence of the metal electrodes gives rise to an increase of the bending stiffness (the area moment $I=bh^3/12$ for Euler-Bernoulli beam, where *h* is the thickness of a beam) in the narrower region. Thus, *G* is assumed to be larger than *H*. To simplify the analysis, we assume that masses are concentrated at the nodes, where the rotational couplers are present. Due to the asymmetry of a half unit cell in the real samples, we also assign different masses, *m* and *M*, to the nodes. We also assume that the dynamic displacement is small enough compared to the film dimension, so that the rotational inertia is negligible. This assumption is also valid in the derivation of the Euler-Bernoulli continuous beam model.

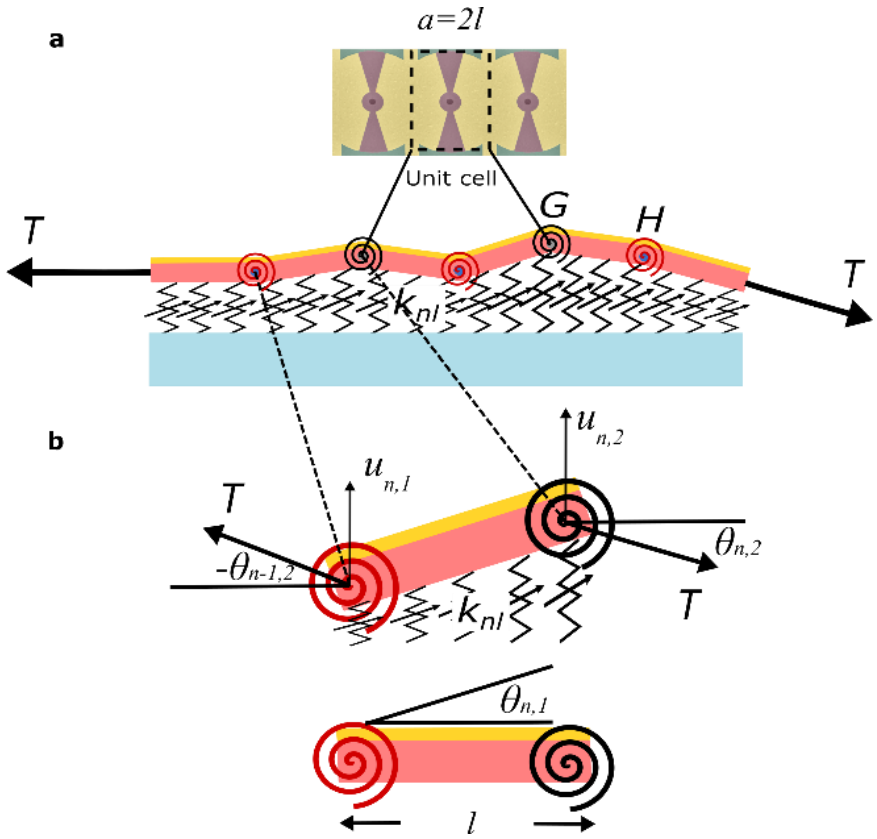

Supplementary Figure 5. Discrete element model of the NEML for analytical calculation of frequency dispersion. (a) Top: Scanning electron microscope image (false colored) showing three unit-cells with the deposited electrodes. Bottom: Schematic diagram of the mass-spring systems used to solve the dynamic model. (b) Close-up view of a half unit cell, showing the two rotational springs connected by a rigid bar, and the elastic foundation. All relevant parameters and degrees of freedom are indicated.

This discrete plate model is more accurate than a usual discrete mass-spring model since the plate model also considers the couplings with next-nearest neighbors. The rotational couplings are

introduced to effectively emulate bending moments in continuous systems. In the long-wavelength limit of the usual discrete mass-spring model, the dispersion relation is linear with $\omega = cq$, where ω, c, and q are the frequency, the linear sound velocity, and a wave number. This is because the nearest neighbor coupling picture leads to d^2u/dx^2 term in the limit. Thus, the optical branch of a dimerized discrete mass-spring model can never be stiffer than its acoustic branch. However, we will see that the experimental and numerical dispersion in our systems exhibit a stiffer optical branch. Such dispersion curves can be modelled by considering rotational springs with discrete beam elements, which lead to $\omega = cq^2$ dispersion relation in the long-wavelength limit. This dispersion stems from the dispersive term d^4u/dx^4. This q^2 dispersion is well-known from the dispersion relation of a continuous Euler-Bernoulli beam.

We start our modeling by calculating the Lagrangian for a single unit cell.

$$
\begin{aligned}
L_n &= T - U_n \\
&= \frac{1}{2} m\dot{u}_{n,1}^2 + \frac{1}{2} M\dot{u}_{n,2}^2 \\
&\quad -[\frac{H}{2}(\theta_{n-1,2} - \theta_{n-1,1})^2 + \frac{G}{2}(\theta_{n,1} - \theta_{n-1,2})^2 + \frac{H}{2}(\theta_{n,2} - \theta_{n,1})^2 + \frac{G}{2}(\theta_{n+1,1} - \theta_{n,2})^2 \\
&\quad + \frac{k_{nl}}{2}\int_0^l \left[u^2{}_{n,1/n-1,2}(x) + u^2{}_{n,2/n,1}(x) + u^2{}_{n+1,1/n,2}(x)\right]dx \\
&\quad + \frac{J}{2}\theta_{n-1,2}^2 + \frac{J}{2}\theta_{n,1}^2 + \frac{J}{2}\theta_{n,2}^2 \\
&\quad + \frac{1}{2}Tl\theta_{n-1,2}^2 + \frac{1}{2}Tl\theta_{n,1}^2 + \frac{1}{2}Tl\theta_{n,2}^2]
\end{aligned}
\tag{S11}
$$

The two terms in the second line are the kinetic energy of each node. The third line represent the rotational coupling of two neighboring plates. The fourth line represents the potential energy stored in the elastic foundations. Here, $u_{i/j}(x) = \frac{u_i - u_j}{l}x + u_j$ is the geometry of a beam in terms of its nodal displacements and x is the local coordinate in the beam. The fifth line describes the on-site rotational coupling. The remaining terms are the effects of tension to single beam rotations. Since the tension terms have the same form with the on-site rotational coupling terms, we let $J_{tot} = J + Tl$. If we assume that the rotational inertia is negligible, we can obtain the equation of motions for $u_{n,1}$ and $u_{n,2}$ by solving Lagrange equation $\frac{d}{dt}\left(\frac{\partial L}{\partial \dot{u}_{n,k}}\right) - \frac{\partial L}{\partial u_{n,k}} = 0$, where k is the node index. Since the beams are connected by a pin, the rotation can be described in terms of the nodal displacement as $\theta_{n,1} = (u_{n,2} - u_{n,1})/l$, and $\theta_{n,2} = (u_{n+1,1} - u_{n,2})/l$.

The equation of motion for the displacement $u_{n,1}$ of n[th] unit cell is

$$\begin{aligned} m\ddot{u}_{n,1} = &-\frac{1}{l^2}[Hu_{n-1,1} - 2(G+H)u_{n-1,2} + 2(H+2G)u_{n,1} \\ &-2(G+H)u_{n,2} + Hu_{n+1,1}] \\ &+\frac{J_{tot}}{l^2}(u_{n-1,2} - 2u_{n,1} + u_{n,2}) \\ &-\frac{k_{nl}l}{6}(u_{n-1,2} + 4u_{n,1} + u_{n,2}) \end{aligned} \quad . \tag{S12}$$

The equation of motion for the displacement $u_{n,2}$ of n[th] unit cell is

$$\begin{aligned} M\ddot{u}_{n,2} = &-\frac{1}{l^2}[Gu_{n-1,2} - 2(G+H)u_{n,1} + 2(2H+G)u_{n,2} \\ &-2(G+H)u_{n+1,1} + Gu_{n+1,2}] \\ &+\frac{J_{tot}}{l^2}(u_{n,1} - 2u_{n,2} + u_{n+1,1}) \\ &-\frac{k_{nl}l}{6}(u_{n,1} + 4u_{n,2} + u_{n+1,1}) \end{aligned} \quad . \tag{S13}$$

We consider traveling solutions $u_{n,1} = Ue^{-j\omega t + jqna}$, $u_{n,2} = Ve^{-j\omega t + jqna}$, which satisfy the Bloch theorem. By inserting the solutions, we obtain an eigenvalue equation $\omega^2\mathbf{Mu} = \mathbf{D}(q)\mathbf{u}$. The mass and the stiffness matrix are given by

$$\mathbf{M} = \begin{bmatrix} m & 0 \\ 0 & M \end{bmatrix}, \quad \mathbf{D}(q) = \begin{bmatrix} D_{11}(q) & D_{12}(q) \\ D_{21}(q) & D_{22}(q) \end{bmatrix},$$

with

$$\begin{aligned} D_{11}(q) &= \frac{2H\cos qa + 2(H+2G)}{l^2} + (\frac{2k_{nl}l}{3} + \frac{2J_{tot}}{l^2}) \\ D_{12}(q) &= \bar{D}_{21}(q) = -2(\frac{G}{l^2} + \frac{H}{l^2} + \frac{J_{tot}}{2l^2} - \frac{k_{nl}l}{12})(1 + e^{-jqa}) \\ D_{22}(q) &= \frac{2G\cos qa + 2(2H+G)}{l^2} + (\frac{2k_{nl}l}{3} + \frac{2J_{tot}}{l^2}) \end{aligned} .$$

The dispersion relation $\omega(q)$ can be obtained by solving the eigenvalue problem.

$$\omega(q)^2 = \frac{mD_{11}(q) + MD_{22}(q) \pm \sqrt{mD_{11}(q) - MD_{22}(q)^2 + 4mMD_{12}(q)D_{21}(q)}}{2mM} \quad \text{(S14)}$$

Based this analytical model, we can qualitatively investigate the contributions of the experimental parameters, such as residual stress and the electrostatic gate tuning, on the frequency dispersion. We now use this model to examine the effects of tension and the on-site potential on the dispersion curves. To match the frequency regions in the experiments, we use manually chosen parameters: m = 3.5×10^{-14} kg/m^3, M = 1.1m, J_{tot} = 5×10^{-10} N.m, l=3.5 μm, and a = 2l.

Figure S6a shows the numerical frequency dispersions for different values of axial tensile residual stress in the lattice. The corresponding analytical dispersions are shown in Figure S7a. We set a constant on-site potential k_{nl} = 50×10^6 N/m^2. An increasing axial residual stress induces the shifting of the dispersion curves, reducing the size of the band gap between acoustic and optical branches. The reduction of the band gap stems from the reduced contrast of the rotational couplings, G and H as described in Figure S7a. One interesting point is the pinning at q = 0 in the acoustic branch. The infinite wavelength mode of the lattice at q = *0* shows the in-phase oscillations of all the rigid plate without rotation. In this case, the tension does not play a role.

Figure S6b shows the numerical dispersion when varying the lattice-perpendicular residual stress. Figure S7b shows the effect of the on-site potential at constant values of the rotational couplings. The increased on-site potential shifts all the branches upward. The width of acoustic branch also decreases as the contributions of the local potential becomes significant compared to the rotational couplings. The contributions of the residual stress are almost equivalent to the on-site of potentials in the analytical model. Such variation of the frequency dispersion is also observed when varying the gate voltage as shown in Figure 2 of the manuscript.

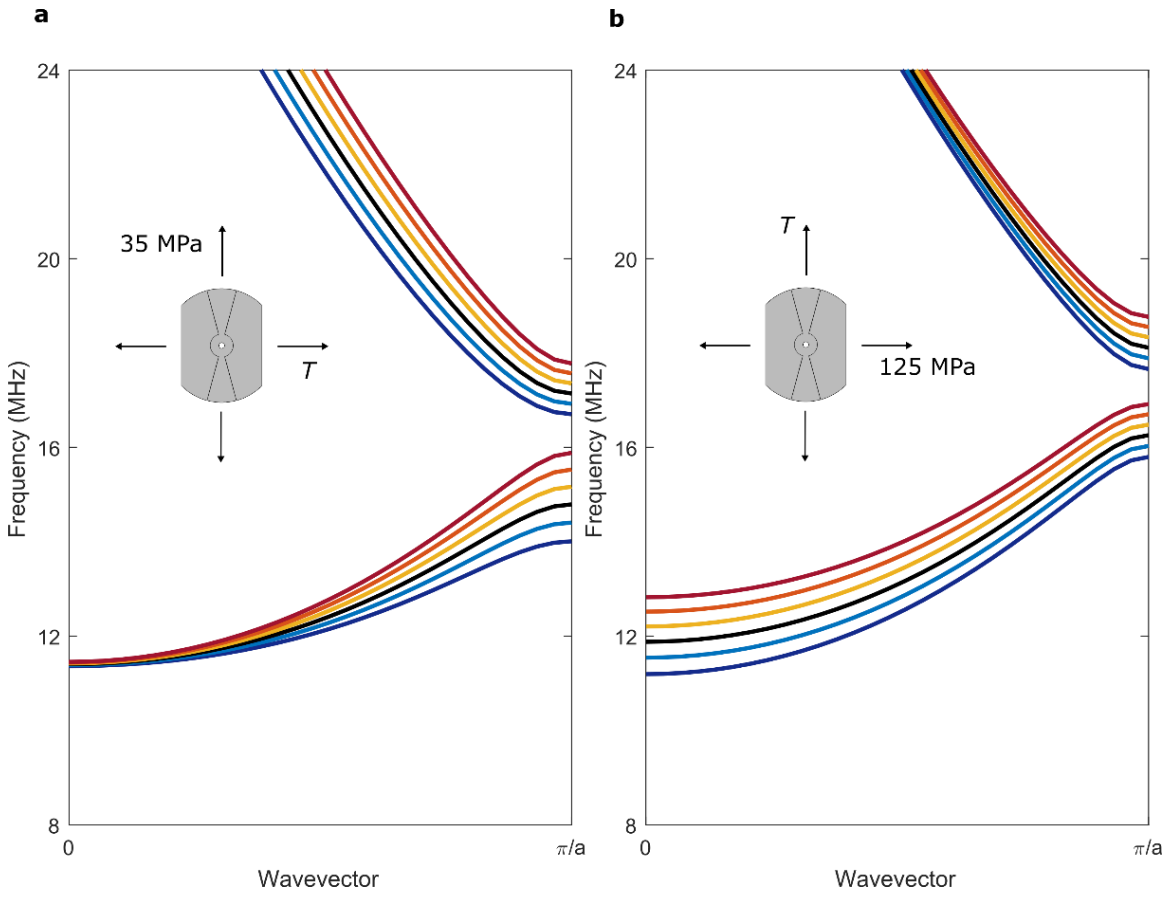

Supplementary Figure 6. Effects of residual stress in the finite element model. (**a**) Numerical dispersion curves for different axial residual stress, *T*. *T* varies from 0 (dark blue) to 120 MPa (dark red) with 20 MPa steps. A constant residual radial stress of 35 MPa is assigned in the direction perpendicular to the lattice. (**b**) Numerical dispersion curves at different lattice-perpendicular residual stresses *T*. *T* varies from 0 (dark blue) to 120 MPa (dark red) with 20 MPa steps.

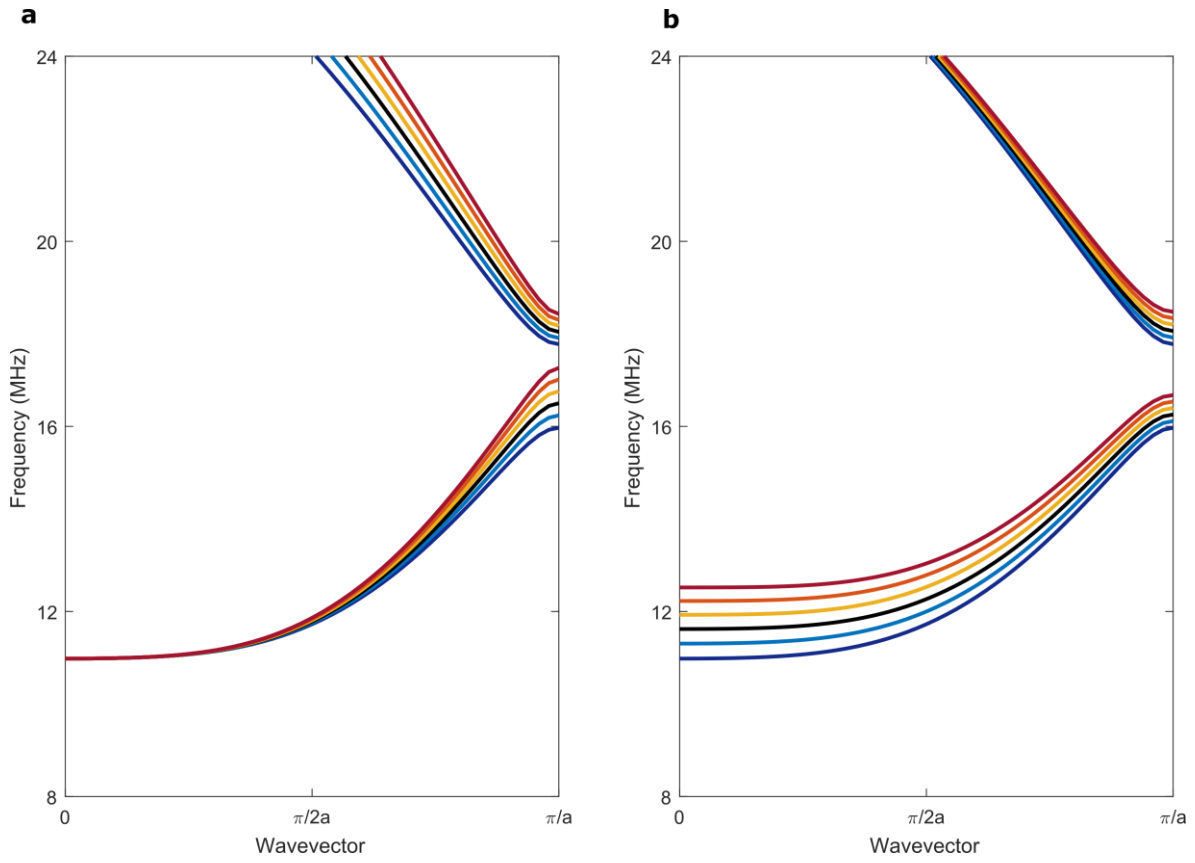

Supplementary Figure 7. Effects of rotational couplings and on-site potential in the analytical model. (**a**) Analytical dispersion curves for different rotational couplings, G and H. G vary from 7.3×10^{-10} N.m (dark blue) to 8.3×10^{-10} N.m (dark red) with 0.2×10^{-10} N.m steps, and H from from 5.8×10^{-10} N.m (dark blue) to 7.8×10^{-10} N.m (dark red) with 0.4×10^{-10} N.m steps with $k_{nl} = 50\times10^{6}$ N/m^2. (**b**) Analytical dispersion curves for different on-site potentials, k_{nl}. k_{nl} varies from 50×10^{6} N/m^2 (dark blue) to 65×10^{6} N/m^2 (dark red) with 3×10^{6} N/m^2 steps. G=7.3×10^{-10} N.m and H=5.8×10^{-10} N.m are fixed.

8. Discussion on the effects of fabrication errors

To investigate the influence of possible fabrication errors, we employ the discrete plate model to perform eigenfrequency analysis on a finite lattice with 120 unit cells varying the systems parameters. We assume that the both ends of the lattice are fixed. The fixed parameters of the model are $m = 3.5\times10^{-14}$ kg/m^3, M = 1.1m, G= 7.3×10^{-10} N.m, H = 5.8×10^{-10} N.m, J_{tot} = 5×10^{-10} N.m, l=3.5 μm, and a = 2l.

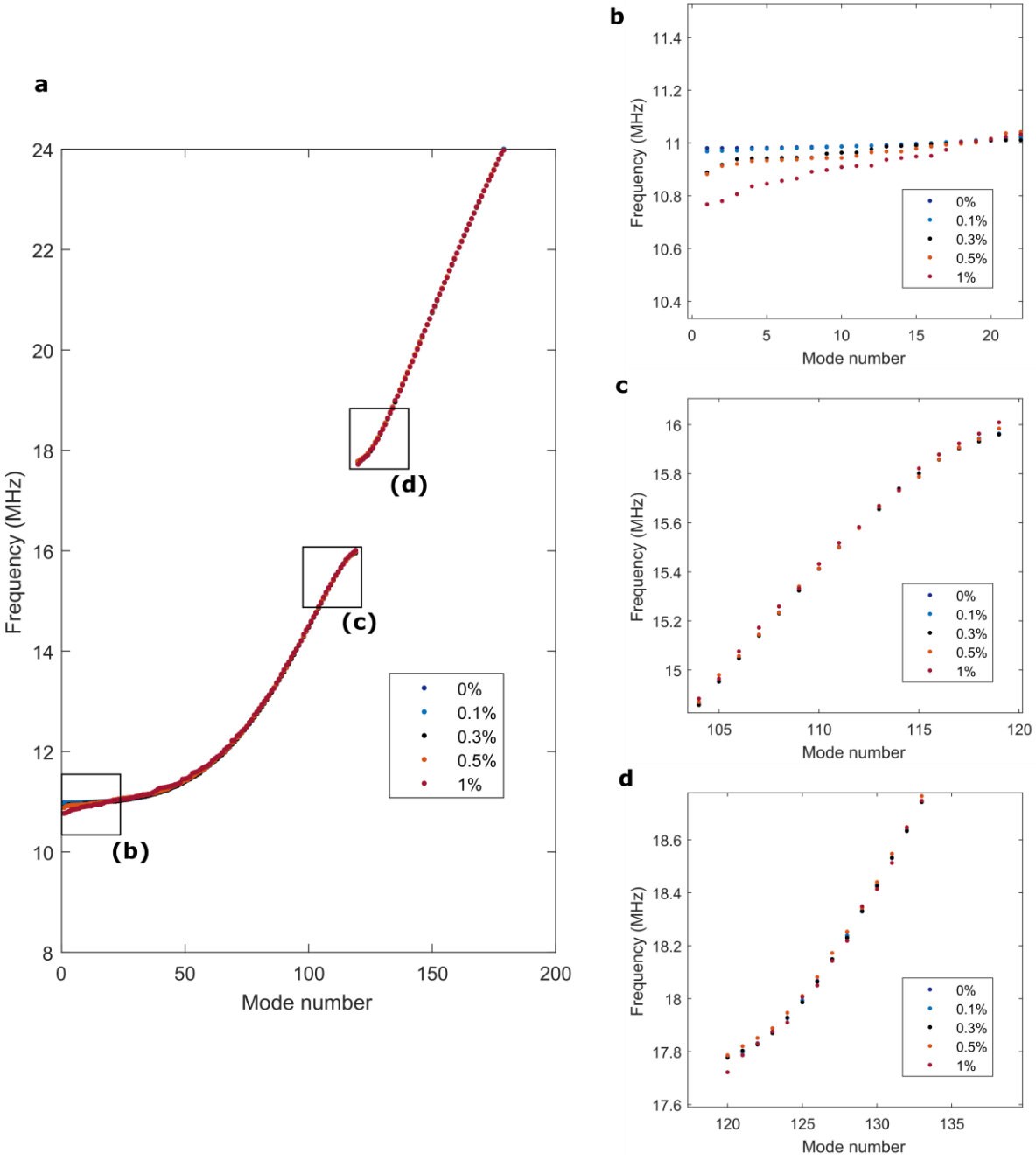

Supplementary Figure 8. Effects of fabrication errors on eigenfrequencies in the analytical model. (**a**) Eigenfrequencies for different error percentages. The regions marked by three black squares are presented in panel (**b),** (**c**), and (**d**).

To model fabrication errors in the study, we vary the percentage of randomness in the value of the masses, rotational couplings, and on-site potentials. Provided that the fabrication errors happen during the deposition process, the non-uniformity in the film thickness causes disorder in the mass matrix in the dynamics equations (Eq. S12 and S13). Considering that the bending

stiffness of the beam elements depends on the cubic of the membrane's thickness, errors in mass lead to cubic errors in the rotational couplings and the on-site potentials. Here we assume that the randomness is governed by a normal distribution, $\sigma N(0,1)$, where σ is an error and $N(0,1)$ is a normal distribution with mean 0 and standard deviation 1.

Figure S8 shows the influences of fabrication errors on the eigenfrequencies. Their range becomes broader as the randomness increases. Especially, the eigenfrequencies near the lower acoustic band edge (Fig. S8b) present more broadening than those near the band gap region (Fig. S8c and S8d). However, when disorder is present, not all eigenfrequencies are extended (or propagating) and localized modes exist for the eigenfrequencies near the band edges.

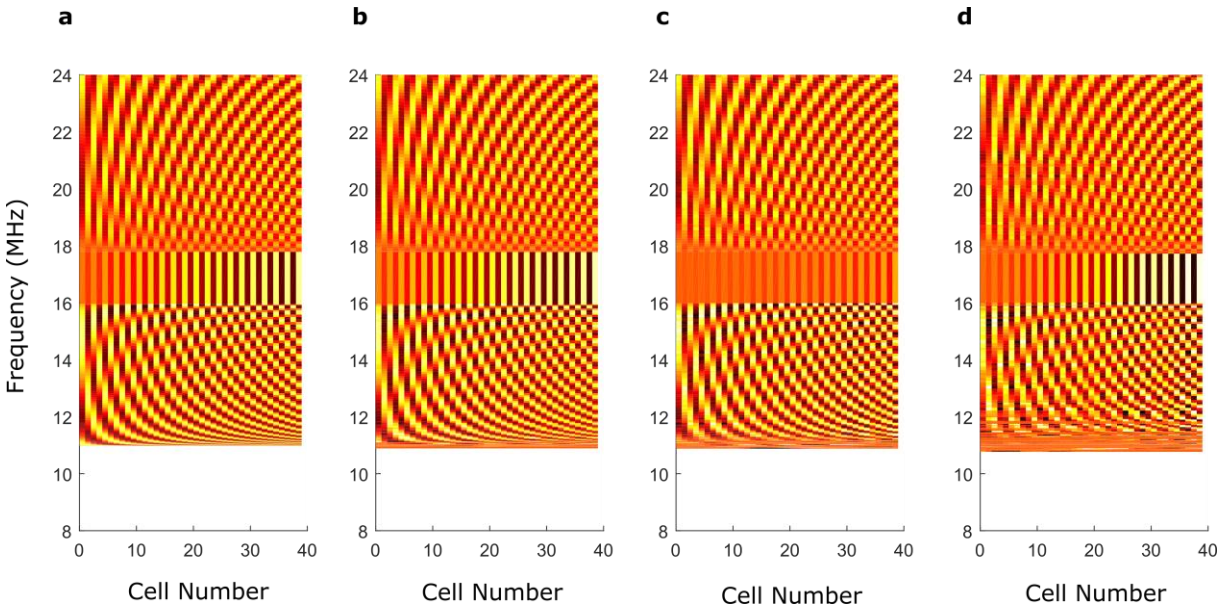

Supplementary Figure 9. Effects of fabrication errors on mode shapes in the analytical model. Mode shapes for (**a**) 0%, (**b**) 0.3%, (**c**) 0.5%, and (**d**) 1% randomness in masses.

To investigate the nature of the eigenmodes, we provide the mode shapes for different eigenfrequencies (Fig. S9). To compare these mode shapes with the ones obtained from experiments (Fig. S4), only mode shapes for the 40 unit cells between the 3rd and the 42nd sites are studied. The mode shapes for a perfect lattice present clear spatial oscillation patterns for different frequencies. As the randomness increases, the spectra become broader, but the localized modes start to appear near the lower acoustic band edge. For 1% disorder (Fig. S9d), the frequency range of the localized modes spans between 11 MHz and 12 MHz. Such localized modes are not easily excited by applying a boundary force, broadening the stop bands.

These spatial oscillation patterns in Figure S9d are different from the observed data in Fig. S4b. This suggests that intrinsic fabrication errors in the devices studied in this work are not playing

a relevant role. The experimental scanning data for V_T = 0 V demonstrates very clear spatial oscillation patterns in the lower acoustic band edges, around 11 MHz, similar to the perfect lattice case from the analytical model (Fig. S9a).

9. Discussion on the dynamic modulation

Figure 4a shows a hardening nonlinear dynamic response with hysteresis. Similar nonlinear behaviors have been observed in nanoelectromechanical systems with clamped boundary conditions [S2]. The hardening behavior mostly stems from an increase of the tension under a strong dynamic excitation, which can be modeled with a cubic nonlinearity in an equivalent mass-spring system [S2]. Moreover, the application of the DC tuning voltage leads to deflection-induced quadratic nonlinearity due to the broken inversion symmetry in equilibrium configurations. Thus, we assume that the quadratic and cubic nonlinearities are present in the elastic foundation, by replacing k_{nl} u with k_1 u + k_2u^2 + k_3u^3.

We analyze the frequency response of the lattice when subject to AC modulations. Figure S10a and S10b show the first harmonic and the second harmonic at different modulation frequencies. As seen in Figure 4a, the amplitude of the first harmonic increases with the modulation frequency ω_p. At ω_p = 11.4 MHz and 11.5 MHz, two side-band responses start to appear. These peaks come from nonlinear resonances [S3]. The nonlinear resonances occur when a driving frequency equals the sum of a pair of normal modes in the lattice. We note that the sum of two side-band frequencies equals $2\omega_p$ (Fig. S10a). We conclude that the second harmonics of the modulation (Fig. S10b) due to an inherent square nonlinearity in the lattice excites the side band of the corresponding first harmonics by nonlinear resonances.

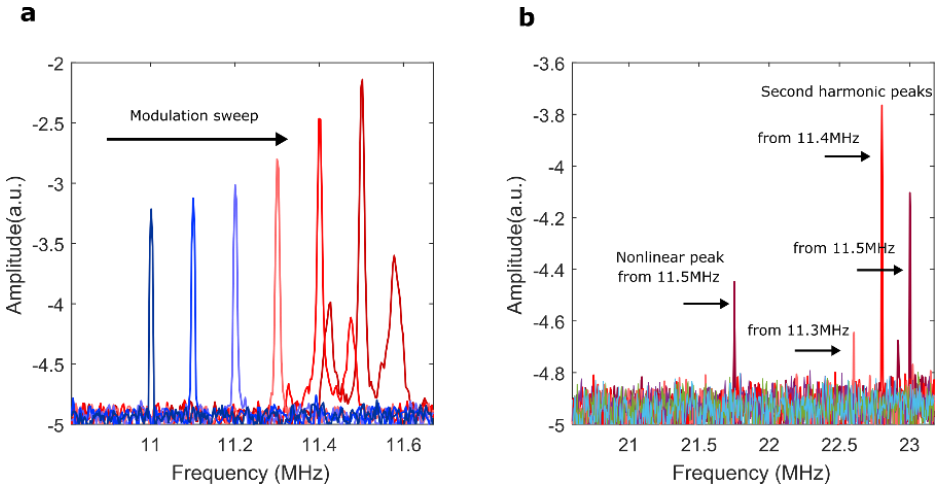

Supplementary Figure 10. Frequency responses of the motion of the lattices under dynamic modulation. (**a**) The first harmonic components of AC modulation. The sweep direction is indicated by an arrow. (**b**) The corresponding second harmonic components.

Here, we focus on the second harmonic component, to unveil the origin of the nonlinear band gap. For this discussion, we study the analytical frequency dispersion curve (Fig. S11a). We note that the second harmonic of the modulation frequency lies around $q = \pi/2a$ (Fig. S11a). The corresponding mode shape at $q = \pi/2a$ (Fig. S11c and S11d) has the wavelength of $4a$. However, if the amplitude of the oscillation is only considered neglecting the phase of the mode, the wavelength of the amplitude is $2a$. Thus, the difference in the amplitudes (light green and red ellipses in Fig. S11c and S11d) within the extended unit cell with $2a$ periodicity (Fig. S11d) induces the dimerization of the lattice, by having dimerized nonlinear elastic foundations. Consequently, the dispersion curves fold at new Brillouin zone boundary, $q = \pi/2a$. In our experiments, we observe the emergence of the nonlinear band gap in the acoustic branch (Fig. 4b and 4c).

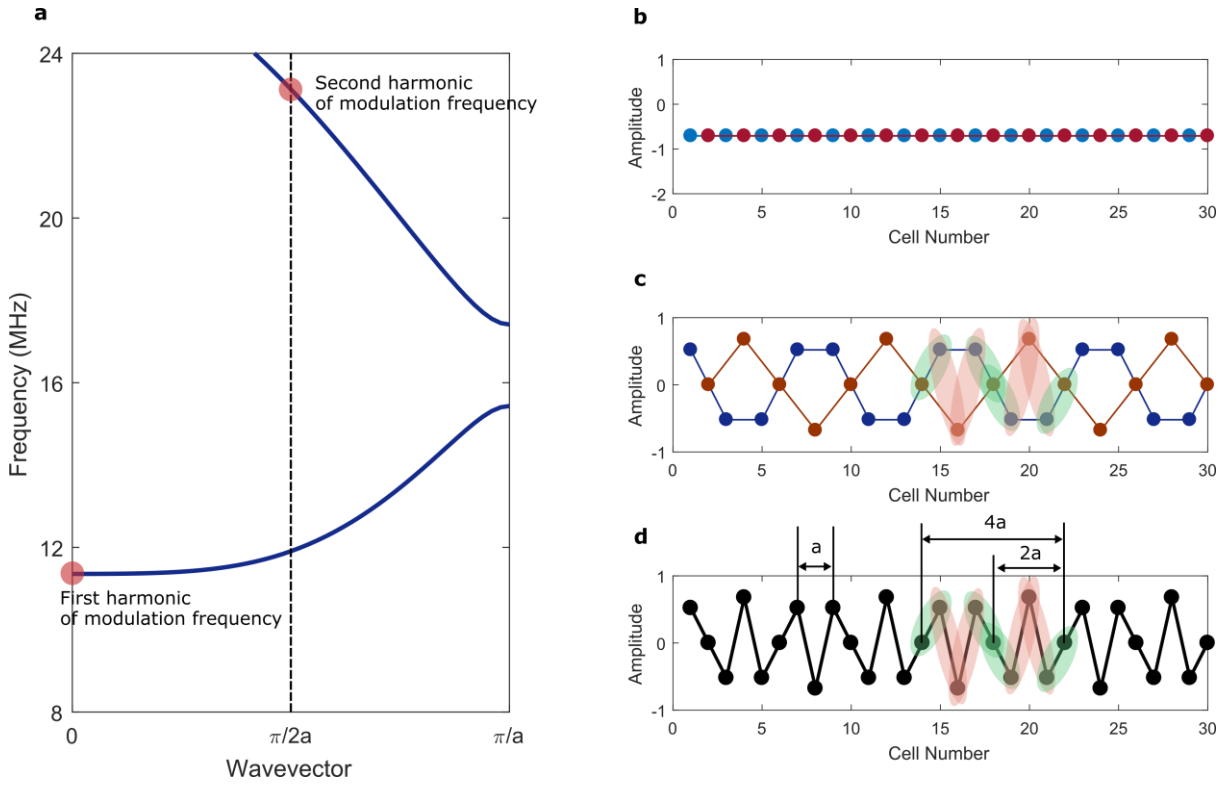

Supplementary Figure 11. Mechanism of the nonlinear band gap formation. (**a**) Schematic dispersion curves obtained from the analytical discrete model. The first harmonic and the second harmonic components of the modulation frequency are marked by red solid circles. (**b**) Mode shape of the first harmonic and (**c**) the second harmonic components in an infinite lattice model. The blue (red) solid circles represent the first (second) node in a unit cell. Note that the unit cell contains two nodal points. (**d**) The real mode shape. Each black solid line represents the rigid plate connecting two neighboring nodes. a is the original periodicity and $2a$ is the modified periodicity due to the nonlinearity. The light red and green ellipses denote the two different amplitude components dimerizing the lattice.

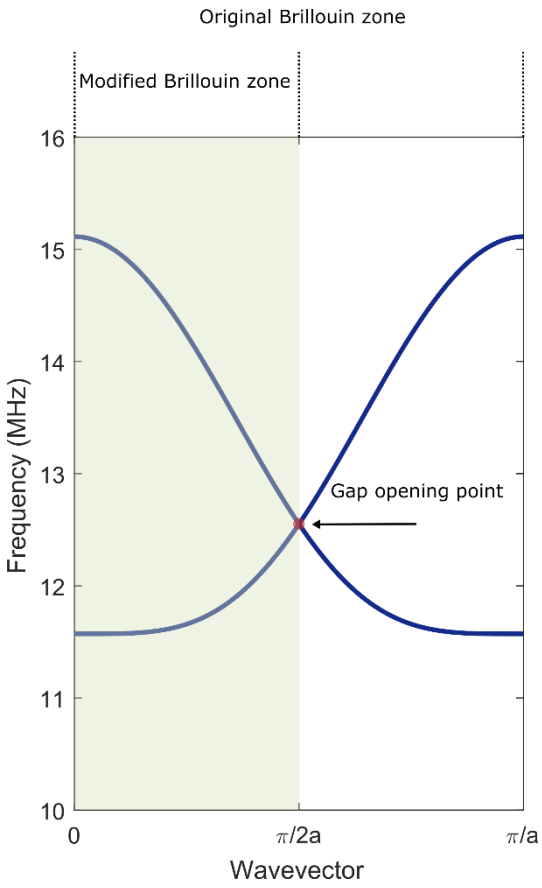

Supplementary Figure 12. Nonlinear dynamically induced Brillouin zone folding of the acoustic branch. Dispersion curves for the acoustic branch from the analytical model. The green shaded area represents the new Brillouin zone, with a gap opening point marked by a red dot.

10. Perturbation analysis for nonlinear band gap

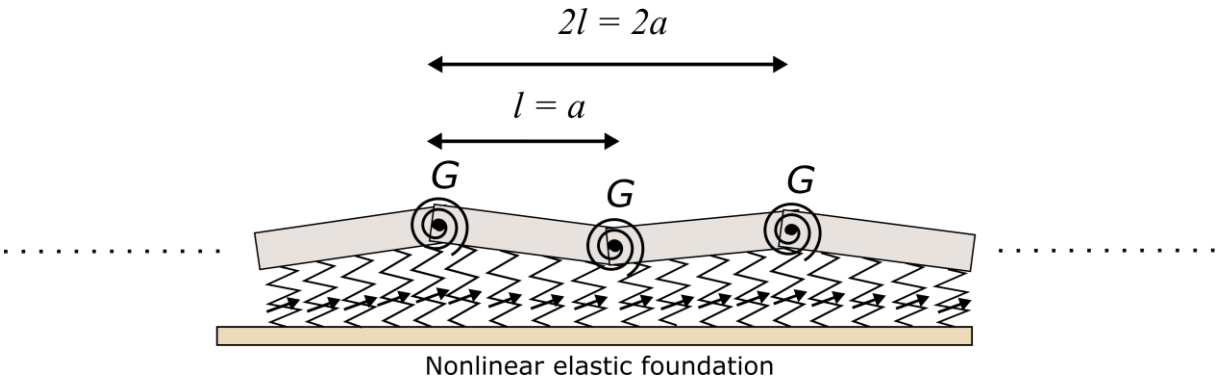

Supplemetary Figure 13. One-dimensional discrete beam lattice for modeling the acoustic branch.

To theoretically study the nonlinear band gap, we perform a classical perturbation analysis of the frequency dispersion. To simplify the problem, we only consider the acoustic branch with a discrete element model consisting of connected rigid beams, of length *l*, on a nonlinear elastic foundation (Fig. S13). Since the experimental results show a band gap opening mechanism at $q= \pi/2a$ (Fig. 4e), we perform our analysis considering a «super-cell» with a 2a periodicity. To further simplify, here we neglect the contributions from the axial tension and the on-site rotational coupling. We model the nonlinear elastic foundations including an additional quadratic and cubic nonlinearities, $k_1 \mathrm{u} + k_2\mathrm{u}^2 + k_3\mathrm{u}^3$. We now show how the nonlinearity in the foundation opens a band gap at the zone-boundary $q= \pi/2a$. The Lagrangian for a unit cell is given by

$$
\begin{aligned}
\sum_i L &= \sum_i (T-U) \\
&= \frac{1}{2} m\dot{u}_{n,1}^2 + \frac{1}{2} m\dot{u}_{n,2}^2 \\
&\quad -[\frac{G}{2}(\theta_{n-1,2}-\theta_{n-1,1})^2 + \frac{G}{2}(\theta_{n,1}-\theta_{n-1,2})^2 + \frac{G}{2}(\theta_{n,2}-\theta_{n,1})^2 + \frac{G}{2}(\theta_{n+1,1}-\theta_{n,2})^2 \\
&\quad + \frac{k_1 l}{2}\int_0^l \left[u^2{}_{n,1/n-1,2}(x) + u^2{}_{n,2/n,1}(x) + u^2{}_{n+1,1/n,2}(x)\right]dx \\
&\quad + \frac{k_2 l}{3}\int_0^l \left[u^3{}_{n,1/n-1,2}(x) + u^3{}_{n,2/n,1}(x) + u^3{}_{n+1,1/n,2}(x)\right]dx \\
&\quad + \frac{k_3 l}{4}\int_0^l \left[u^4{}_{n,1/n-1,2}(x) + u^4{}_{n,2/n,1}(x) + u^4{}_{n+1,1/n,2}(x)\right]dx]
\end{aligned}
\qquad \text{. (S15)}
$$

Here, we skip the detailed description of each term. Using the Lagrange equation of motion, we derive the following equations for the two beams in a unit cell:

$$\frac{d}{dt}\left(\frac{\partial L}{\partial \dot{u}_{i,1}}\right)-\frac{\partial L}{\partial u_{i,1}}=0$$

$$\begin{aligned} m\ddot{u}_{i,1} = &-\frac{1}{l^2}[Gu_{i-1,1}-4Gu_{i-1,2}+6Gu_{i,1}-4Gu_{i,2}+Gu_{i+1,1}] \\ &-\frac{k_1 l}{6}(u_{n-1,2}+4u_{n,1}+u_{n,2}) \\ &-\frac{k_2 l}{12}(u^2{}_{n-1,2}+2u_{n-1,2}u_{n,1}+6u^2{}_{n,1}+2u_{n,1}u_{n,2}+u^2{}_{n,2}) \\ &-\frac{k_3 l}{20}(u^3{}_{n-1,2}+2u^2{}_{n-1,2}u_{n,1}+3u_{n-1,2}u^2{}_{n,1}+8u^3{}_{n,1}+3u^2{}_{n,1}u_{n,2} \\ &+2u_{n,1}u^2{}_{n,2}+u^3{}_{n,2}) \end{aligned} , \tag{S16}$$

$$\frac{d}{dt}\left(\frac{\partial L}{\partial \dot{u}_{i,2}}\right)-\frac{\partial L}{\partial u_{i,2}}=0$$

$$\begin{aligned} m\ddot{u}_{i,2} = &-\frac{1}{l^2}[Gu_{i-1,2}-4Gu_{i,1}+6Gu_{i,2}-4Gu_{i+1,1}+Gu_{i+1,2}] \\ &-\frac{k_1 l}{6}(u_{n,1}+4u_{n,2}+u_{n+1,1}) \\ &-\frac{k_2 l}{12}(u^2{}_{n,1}+2u_{n,1}u_{n,2}+6u^2{}_{n,2}+2u_{n,2}u_{n+1,1}+u^2{}_{n+1,1}) \\ &-\frac{k_3 l}{20}(u^3{}_{n,1}+2u^2{}_{n,1}u_{n,2}+3u_{n,1}u^2{}_{n,2}+8u^3{}_{n,2}+3u^2{}_{n,2}u_{n+1,1} \\ &+2u_{n,2}u^2{}_{n+1,1}+u^3{}_{n+1,1}) \end{aligned} . \tag{S17}$$

Here, we consider the nonlinear terms as a perturbation, which can be scaled by a scaling parameter ε. For the perturbation analysis, we employ the Poincare-Lindstedt method [S4]. We express the eigenfrequency and the displacement as $\omega=\omega_0+\varepsilon\omega_1$ and $\mathbf{u}=\mathbf{u}^{(0)}+\varepsilon\mathbf{u}^{(1)}$, where ω_0 and $\mathbf{u}^{(0)}$ are the eigenfrequency and the corresponding eigenvectors for the unperturbed or linear system. We also introduce a new time variable, $\tau=\omega t$ which leads to $\frac{d^2}{dt^2}=\omega^2\frac{d^2}{d\tau^2}$. In a matrix form, the equation of motion can be described as

$$\mathbf{M}\ddot{\mathbf{u}}=\mathbf{D}(q)\mathbf{u}+\varepsilon\mathbf{K}_{nl}(\mathbf{u}), \tag{S18}$$

with

$$\mathbf{D}(q)=\begin{bmatrix} -\frac{G}{l^2}[e^{-iq2a}+e^{iq2a}+6]-\frac{2k_1l}{3} & (\frac{4G}{l^2}-\frac{k_1l}{6})[e^{-iq2a}+1] \\ (\frac{4G}{l^2}-\frac{k_1l}{6})[e^{iq2a}+1] & -\frac{G}{l^2}[e^{-iq2a}+e^{iq2a}+6]-\frac{2k_1l}{3} \end{bmatrix},$$

and

$$\mathbf{K}_{nl}(\mathbf{u})=\mathbf{K}_1(\mathbf{u})+\mathbf{K}_2(\mathbf{u}),$$

with

$$\mathbf{K}_1(\mathbf{u})=-\frac{k_2l}{12}\begin{bmatrix} u^2{}_{n-1,2}+2u_{n-1,2}u_{n,1}+6u^2{}_{n,1}+2u_{n,1}u_{n,2}+u^2{}_{n,2} \\ u^2{}_{n,1}+2u_{n,1}u_{n,2}+6u^2{}_{n,2}+2u_{n,2}u_{n+1,1}+u^2{}_{n+1,1} \end{bmatrix},$$

$$\mathbf{K}_2(\mathbf{u})=-\frac{k_3l}{20}\begin{bmatrix} u^3{}_{n-1,2}+2u^2{}_{n-1,2}u_{n,1}+3u_{n-1,2}u^2{}_{n,1}+8u^3{}_{n,1}+3u^2{}_{n,1}u_{n,2}+2u_{n,1}u^2{}_{n,2}+u^3{}_{n,2} \\ u^3{}_{n,1}+2u^2{}_{n,1}u_{n,2}+3u_{n,1}u^2{}_{n,2}+8u^3{}_{n,2}+3u^2{}_{n,2}u_{n+1,1}+2u_{n,2}u^2{}_{n+1,1}+u^3{}_{n+1,1} \end{bmatrix}.$$

After the perturbation analysis, we set ε =1 so that we can recover the original equations of motion. By inserting the perturbed eigenfrequency, ω, and the displacement, $\mathbf{u}^{(0)}$, and organizing the equations according to the order of the perturbation parameter, we have

$$O(\varepsilon^0):\omega_0{}^2\mathbf{M}\frac{d^2\mathbf{u}^{(0)}}{d\tau^2}=\mathbf{D}(q)\mathbf{u}^{(0)}, \tag{S19}$$

$$O(\varepsilon^1):\omega_0{}^2\mathbf{M}\frac{d^2\mathbf{u}^{(1)}}{d\tau^2}-\mathbf{D}(q)\mathbf{u}^{(1)}=-2\omega_0\omega_1\mathbf{M}\frac{d^2\mathbf{u}^{(0)}}{d\tau^2}+\mathbf{K}_1(\mathbf{u}^{(0)})+\mathbf{K}_2(\mathbf{u}^{(0)}). \tag{S20}$$

The solution to Equation A3.5 can be assumed as

$$\mathbf{u}_n^{(0)}=\frac{1}{2}[\mathbf{U}e^{i(2qna+\tau)}+\mathbf{U}e^{-i(2qna+\tau)}]=\mathbf{U}\cos(2qna+\tau),\quad \mathbf{U}=\begin{bmatrix}x\\y\end{bmatrix}.$$

By inserting the solution to Equation S20, we have static and second harmonic terms from the quadratic nonlinearity, and the first harmonic and third harmonic terms from the cubic nonlinarity. These terms act as source terms in the nonhomogeneous ordinary differential equation, Equation S20. However, the eigenfrequencies of the equation are identical to those of the unperturbed equation (Eq. S19). Therefore, the first order frequency shift can be obtained by setting the secular

term, soely originated from the cubic nonlinearity, to be zero. At the folded zone boundary, $q= \pi/2a$, the condition can be written as

$$2\omega_0\omega_1\mathbf{M}\begin{bmatrix}x\\y\end{bmatrix}-\frac{k_3 l}{20}\begin{bmatrix}3x^3+\dfrac{3xy^2}{2}\\3y^3+\dfrac{3x^2y}{2}\end{bmatrix}=0\,.$$

Thus, there are two solutions for the first order perturbation frequency,

$$\omega_1=\frac{3k_3 l}{40\omega_0 m}[3x^2+\frac{3y^2}{2}]\ ,\ \text{and}\quad \omega_1=\frac{3k_3 l}{40\omega_0 m}[3y^2+\frac{3x^2}{2}]. \tag{S21}$$

The difference of the two perturbation frequencies is the nonlinear band gap, which is expressed as

$$\Delta\omega=\frac{9k_3 l}{80\omega_0 m}\left|x^2-y^2\right|. \tag{S22}$$

This equation states that the new band gap $\Delta\omega$ is amplitude dependent and can be opened if nonlinearities are present in the system. As seen in the mode shapes (Fig. S11), the band gap can be opened when there is an asymmetry in the nodal displacements *x* (red ellipses) and *y* (green ellipses). Also, the size of the band gap depends on the nonlinear coefficient k_3.

References

S1. Mamabili, M. Nonlinear vibrations and stability of shells and plates. Cambridge (2008)

S2. Schmid, S., Villanueva, L. G., Roukes, M.L. Fundamentals of nanomechanical resonators. Springer (2016)

S3. Cao, L. S., Qi, D. X., Peng, R. W., Wang, M., Schmelcher, P. Phononic frequency combs through nonlinear resonances. *Phys. Rev. Lett.* **112**, 075505 (2014)

S4. Nayfeh, A. H., Mook, D. T. Nonlinear oscillations. Wiley (1995)